

# Shape-Directed Microspinners Powered by Ultrasound

Syeda Sabrina,<sup>†</sup> Mykola Tasinkevych,<sup>§,¶</sup> Suzanne Ahmed,<sup>‡</sup> Allan M. Brooks,<sup>†</sup> Monica Olvera de la Cruz,<sup>||</sup> Thomas E. Mallouk,<sup>‡</sup> and Kyle J. M. Bishop<sup>\*,†,⊥</sup>

<sup>†</sup>Department of Chemical Engineering and <sup>‡</sup>Department of Chemistry, The Pennsylvania State University, University Park, Pennsylvania 16802, United States

<sup>§</sup>Department of Materials Science and Engineering and <sup>||</sup>Department of Chemistry, Northwestern University, Evanston, Illinois 60208, United States

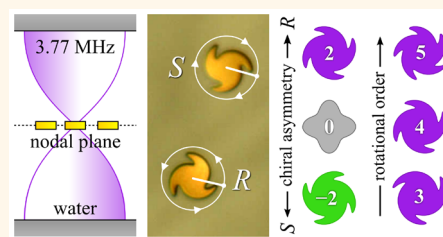
<sup>⊥</sup>Department of Chemical Engineering, Columbia University, New York, New York 10027, United States

<sup>¶</sup>Centro de Física Teórica e Computacional, Departamento de Física, Faculdade de Ciências, Universidade de Lisboa, Campo Grande P-1749-016 Lisboa, Portugal

## Supporting Information

**ABSTRACT:** The propulsion of micro- and nanoparticles using ultrasound is an attractive strategy for the remote manipulation of colloidal matter using biocompatible energy inputs. However, the physical mechanisms underlying acoustic propulsion are poorly understood, and our ability to transduce acoustic energy into different types of particle motions remains limited. Here, we show that the three-dimensional shape of a colloidal particle can be rationally engineered to direct desired particle motions powered by ultrasound. We investigate the dynamics of gold microplates with twisted star shape ( $C_{nh}$  symmetry) moving within the nodal plane of a uniform acoustic field at megahertz frequencies. By systematically perturbing the parametric shape of these “spinners”, we quantify the relationship between the particle shape and its rotational motion. The experimental observations are reproduced and explained by hydrodynamic simulations that describe the steady streaming flows and particle motions induced by ultrasonic actuation. Our results suggest how particle shape can be used to design colloids capable of increasingly complex motions powered by ultrasound.

**KEYWORDS:** active colloids, acoustic propulsion, acoustic streaming, symmetry, shape



The symmetry of active colloidal particles can be used to direct their motion through viscous environments powered by chemical fuels or external fields.<sup>1–3</sup> A canonical example is the autonomous motion of bimetallic nanorods in hydrogen peroxide solutions ( $C_{\infty v}$  symmetry),<sup>4,5</sup> which swim by means of reaction-induced self-electrophoresis.<sup>6,7</sup> More generally, self-phoretic particles rely on asymmetry in their surface activity and/or phoretic mobility to create local fields that drive particle motions.<sup>8</sup> By breaking the axial symmetry of such particles (e.g., to  $C_s$  symmetry), additional motions such as particle rotation are readily achieved.<sup>9,10</sup> The desired particle asymmetries are most often realized using heterogeneous surface chemistries such as that of bimetallic nanorods<sup>4</sup> or platinum Janus particles;<sup>11</sup> however, asymmetries in particle shape alone are also capable of directing the motions of self-phoretic particles.<sup>12</sup>

Importantly, the use of particle shape to direct the motion of active colloids is generally applicable to any energy input or propulsion mechanism. Alternating electric fields drive translational motions of asymmetric colloidal dimers ( $C_{\infty v}$  symmetry) as well as rotational motions of dimer assemblies

( $C_{nh}$  symmetry) by directing field-induced flows.<sup>13</sup> Light-induced heating of asymmetric microgears ( $C_{6h}$  symmetry) at liquid interfaces induces thermocapillary flows that drive rotational particle motions.<sup>14</sup> Vibrational excitation of an asymmetric, two-sphere swimmer ( $C_{\infty v}$  symmetry) leads to steady streaming flows that drive its linear translational motion.<sup>15</sup> In these examples, particle motion is driven not by external forces or torques but by steady fluid flows induced by the external field and directed by the asymmetric particle shape.

Recently, the propulsion of micro- and nanoparticles using ultrasound has emerged as a promising strategy for the remote manipulation of colloidal matter using biocompatible energy inputs.<sup>16–25</sup> Ultrasonic propulsion can offer rapid particle motions at low input power as well as tunable control over particle activity in space and time. While the details of the propulsion mechanism(s) remain uncertain, one likely

Received: January 19, 2018

Accepted: March 6, 2018

Published: March 16, 2018

contribution comes from asymmetric acoustic streaming, whereby the primary oscillatory flow around an asymmetric particle induces steady secondary flows that drive particle motion.<sup>26</sup> Consistent with this mechanism, recent experiments have revealed that particle shape plays an important role in directing motions powered by ultrasound.<sup>19</sup> In particular, asymmetric nanorods with both concave and convex ends were observed to translate toward their concave end at speeds of approximately 200  $\mu\text{m/s}$ . Building on this insight, we sought to explore how particle shape might be used to direct other types of particle motion powered by ultrasound. In particular, we hypothesized that particles with  $n$ -fold rotational symmetry should be capable of rotational motions in both clockwise (CW) and counterclockwise (CCW) directions. Such bidirectional in-plane rotation is difficult to achieve with torque-driven particles,<sup>27–29</sup> which tend to rotate in a common direction. Ensembles of counter-rotating particles or “spinners” may prove useful in exploring the complex collective dynamics predicted for such active mixtures.<sup>30–34</sup>

Here, we investigate the dynamics of gold microplates with twisted star shape ( $C_{nh}$  symmetry) moving within the nodal plane of a uniform acoustic field at megahertz frequencies. We show that the chiral shape of the particles directs their steady rotation in either the CW or CCW direction, depending on the chiral sense of the particle. By systematically perturbing the parametric shape of these spinners, we describe how the magnitude and direction of rotation depends on the extent of chiral asymmetry, the order of rotational symmetry (*i.e.*, the number of “fins”), and the size of the particles. The experimental observations are reproduced and explained by hydrodynamic simulations that describe the steady streaming flows and particle motions induced by ultrasonic actuation. The simulations reveal that the particle dynamics exhibit sensitive dependence on particle shape when—as in experiment—the particle’s geometric features are commensurate with the boundary layer thickness. Under these conditions, small changes in shape can lead to qualitatively different motions such as reversal in the direction of rotation. Taken together, the experimental observations and model predictions suggest how particle shape can be used to design colloids capable of increasingly complex motions powered by ultrasound. Such shape-encoded particles are of interest as active components within dynamic (dissipative) assemblies—so-called colloidal machines<sup>31</sup>—that organize in space and time to perform useful functions.<sup>35–38</sup>

## RESULTS AND DISCUSSION

Our experiments were performed in a cylindrical acoustic chamber (180  $\mu\text{m}$  in height, 5 mm in diameter) containing an aqueous dispersion of gold microplates of prescribed shape (Figure 1a). The star-shaped particles (150 nm thick, 5.8–23  $\mu\text{m}$  in diameter) were fabricated by projection photolithography followed by thermal evaporation. The shape of the particle perimeter was prescribed by the following parametric equations for a plane curve in polar coordinates:

$$r(s) = a[1 + b \cos(ns)] \text{ and } \theta(s) = s + \frac{c}{n} \cos(ns) \quad (1)$$

where  $0 \leq s \leq 2\pi$  is the parameter. This representation defines a twisted star ( $C_{nh}$  symmetry) of mean radius  $a$  with  $n$  fin-shaped arms each of scaled length  $b = 0.3$ . When confined to a plane normal to the  $n$ -fold symmetry axis, such particles adopt one of two distinct orientations which are mirror images of one

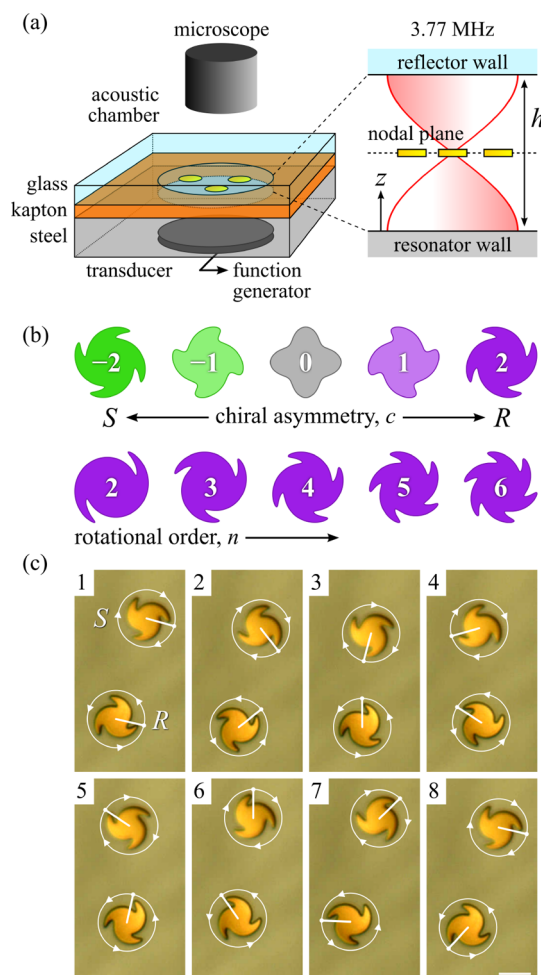


**Figure 1.** (a) Schematic illustration of the acoustic chamber. The magnified region shows a cross section of the chamber with the gold particles levitating at the nodal plane. (b) Particle shapes defined by eq 1 for different values of the chiral asymmetry  $c$  (top, with  $n = 4$ ) and the rotational order  $n$  (bottom, with  $c = 2$ ). (c) Image sequence showing a pair of counter-rotating spinners with  $a = 5.8 \mu\text{m}$ ,  $c = \pm 2$ , and  $n = 3$  (see also Supporting Movie 1). Here, the R spinner rotates CCW, and the S spinner rotates CW. The time interval between successive frames is 1.17 s; the scale bar is 10  $\mu\text{m}$ .

another. The quantity  $c$  describes the direction and magnitude of this chiral asymmetry (Figure 1b). We denote particles with  $c > 0$  as “R” and those with  $c < 0$  as “S” by analogy to chemical convention; particles with  $c = 0$  are achiral ( $D_{nh}$  symmetry). To clarify, none of the particles are chiral in three dimensions; the designation of R or S depends on the perspective of the observer (here, the microscope). For the present experiments, we prepared both symmetric ( $c = 0$ ) and asymmetric ( $c = \pm 1, \pm 2$ ) particles of different sizes ( $a = 2.9, 5.8, \text{ and } 11.5 \mu\text{m}$ ) with different numbers of fins ( $n = 2, 3, 4, 5, \text{ and } 6$ ).

The acoustic chamber was actuated from below by a piezoelectric transducer at a resonant frequency of 3.77 MHz, such that the acoustic wavelength was comparable to twice the height of the chamber  $h$ . As described in previous studies,<sup>16,19</sup> the standing acoustic wave caused the rapid migration of gold particles to the nodal plane ( $z = h/2$ ), at which pressure oscillations were minimal. The plate-like particles oriented their rotation axis normal to the levitation plane and were never observed to reverse orientation (*i.e.*, transitions  $R \rightarrow S$  or  $S \rightarrow R$

were prohibited). So confined within the levitation plane, particles rotated steadily in either the CW or CCW direction depending on their chiral sense (*R* or *S*) as observed by optical microscopy. Otherwise identical particles of opposite sense rotated in opposite directions when subjected to the same acoustic stimulus (Figure 1c; Supporting Movie 1). Achiral particles with  $c = 0$  showed no systematic rotation (Supporting Movie 2).

From the videos, we tracked the spinner orientation with respect to the lab frame as a function of time (Figure 2). The

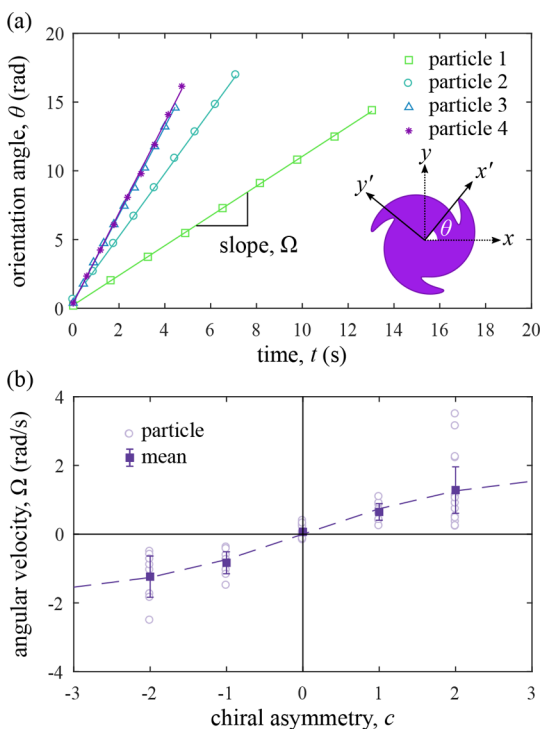


**Figure 2.** (a) Orientation angle  $\theta$  vs time for four *R* spinners with  $n = 3$ ,  $c = 2$ , and  $a = 11.5 \mu\text{m}$ . Solid lines are best linear fits to the data; the slope of the lines represents the angular velocity  $\Omega$ . (b) Angular velocity  $\Omega$  vs chiral asymmetry  $c$  for 3-finned spinners with radius  $a = 11.5 \mu\text{m}$ . Open markers denote measurements on individual particles; solid markers show the mean velocity for a given asymmetry. Error bars represent 95% confidence intervals for the mean angular velocity. The dashed curve is a sigmoidal fit highlighting the symmetry of the data,  $\Omega(-c) = -\Omega(c)$ .

orientation angle  $\theta$  increased linearly in time as  $\theta = \Omega t$ , indicating a constant angular velocity  $\Omega$  independent of particle orientation. By convention, a positive angular velocity corresponds to rotation in the CCW direction when viewed from above. Measurements conducted on different spinners of identical size, shape, and chiral sense revealed variations in the angular velocity depending on the particle's location in the nodal plane (Supporting Movie 3). Similar variations in particle motion were reported previously for acoustically propelled nanorods<sup>19</sup> and attributed to spatial heterogeneity of the pressure field within the levitation plane (so-called nodal structure). Because spinners rotated at a constant rate, it was convenient to measure the angular velocity by counting the number of complete rotations  $N$  within an observation period  $T$  such that  $\Omega = 2\pi N/T$ ; the values of  $\Omega$  reported below were determined in this way.

**Role of Chiral Asymmetry  $c$ .** The speed and direction of rotation depends on the chirality of the particles. Figure 2b shows the angular velocity for 3-finned spinners of radius  $a = 11.5 \mu\text{m}$  as a function of their chiral asymmetry  $c$ . The angular velocity is an odd function of the asymmetry parameter,  $\Omega(-c) = -\Omega(c)$ , and the rotation speed increases monotonically with the magnitude of chiral asymmetry. In these experiments, particles of opposite chiral sense were obtained by fabricating *R* particles and distributing them on the levitation plane with random orientations (*R* or *S*). A particle in the *S* orientation rotates with the same speed but opposite direction as an identical particle in the *R* orientation. This symmetry is not guaranteed owing to the asymmetry of the particle fabrication process and of the acoustic chamber. In other words, the “top” and “bottom” of both the particle and the chamber are, in fact, distinct. In practice, however, such asymmetries were not significant.

For these 3-finned spinners, the direction of rotation was CCW for *R* spinners and CW for *S* spinners; in both cases, the fins traveled toward their concave side. Similar behaviors were reported for asymmetric gold nanorods with convex and concave features at their respective ends.<sup>19</sup> Such nanorods moved reliably toward their concave ends when subject to similar acoustic stimuli. We therefore expected particles with different numbers of fins to behave in a similar manner; they did not.

**Role of Rotational Order  $n$ .** Surprisingly, the direction of particle rotation depends on the order of rotational symmetry—that is, on the number of fins  $n$ . Figure 3a shows

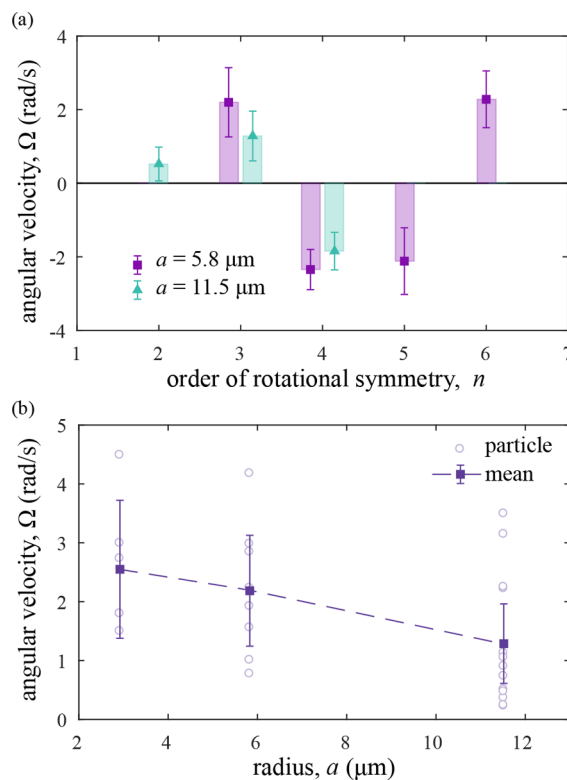


**Figure 3.** (a) Angular velocity  $\Omega$  vs order of rotational symmetry  $n$  for *R* chiral spinners with  $c = 2$ . The error bars show the 95% confidence interval. (b) Angular velocity  $\Omega$  as a function of size  $a$  of the *R* chiral spinners with  $n = 3$  and  $c = 2$ . The error bars show the 95% confidence interval.

that spinners with two-, three-, and six-fold rotational symmetry ( $n = 2, 3,$  and  $6$ ) all rotate in the same direction with the fins moving toward their concave side (CCW rotation for  $R$  spinners). By contrast, spinners with four- and five-fold rotational symmetry ( $n = 4$  and  $5$ ) rotate in the opposite direction with the fins moving toward their convex side (CW rotation for  $R$  spinners). The speed of particle rotation was independent of the number of fins to within experimental uncertainty (e.g.,  $\Omega \approx \pm 2$  rad/s for  $a = 5.8 \mu\text{m}$  and  $c = \pm 2$ ).

Why does the direction of rotation vary non-monotonically with the number of fins? We hypothesized that the rotation direction was determined by some characteristic length of the particle shape—for example, the distance between fin tips. Depending on this length, the particle would interact differently with the surrounding acoustically driven flows, which are characterized by another length scale,  $\sqrt{\nu/\omega} \sim 0.2 \mu\text{m}$ , where  $\nu$  is the kinematic viscosity of water. However, experiments using particles of different sizes did not support this hypothesis. Particles of different size (different  $a$ ) but the same rotational order (same  $n$ ) rotated in the same direction. For example, Figure 3a shows how particles of two different sizes ( $a = 5.8$  and  $11.5 \mu\text{m}$ ) reverse direction from CCW to CW rotation upon increasing the number of fins from  $n = 3$  to  $4$ .

**Role of Size  $a$ .** Whereas the particle size did not influence the direction of rotation, it did impact the speed of rotation. For the range of particle sizes used here ( $a = 2.9\text{--}11.5 \mu\text{m}$ ), we observed that smaller spinners rotate faster than larger spinners (Figure 3b); however, the dependence of speed on size is weak within the limited range of sizes investigated. For 3-finned spinners, a 4-fold increase in particle size resulted in a decrease in the rotation speed by a factor of *ca.* 2. Our observations are in qualitative agreement with those of acoustically propelled nanorods, where propulsion speed is inversely related to the length of the rods.<sup>19</sup> Gold nanorods  $4.7 \mu\text{m}$  in length swam with an average speed of  $11 \mu\text{m/s}$ , which increased *ca.*  $1.6\times$  as the length was decreased by a factor of 3.4.<sup>19</sup>

**Mechanism of Acoustic Rotation.** One likely mechanism for the observed particle motions is asymmetric acoustic streaming—that is, steady fluid flows induced by oscillatory particle motions relative to the surrounding fluid. This mechanism has been investigated previously by Nadal and Lauga<sup>26</sup> to explain the translational motions of gold nanorods at the nodal plane of a standing acoustic wave.<sup>16</sup> Building on their model, we performed numerical simulations of the hydrodynamic flows around the particle induced by its interactions with the acoustic field (see Methods). In contrast to previous analytical studies,<sup>26</sup> our numerical approach allowed us to simulate the motions of complex anisotropic particles at frequencies most relevant to the present experiments. As detailed below, this model is capable of explaining most (but not all) of the key experimental observations. The remaining deviations between model and experiment should be useful in directing future work to better understand acoustic propulsion.

In the model, we consider plate-like particles of prescribed shapes positioned at the nodal plane of a standing acoustic wave. The acoustic field imposes an oscillating velocity field oriented in the  $z$ -direction,  $\mathbf{u}(\mathbf{x}, t) = u^\infty \mathbf{e}_z \cos(\omega t)$ . Owing to the high density of gold, the particle is approximately stationary, and the fluid flows around it in an oscillatory fashion. Due to the high frequency of the acoustic oscillations, the Reynolds number,  $\text{Re} = au^\infty/\nu$ , is not much smaller than one, and inertial effects cannot be neglected. Starting from the Navier–Stokes equations, we use perturbation theory to compute the fluid

flows and particle motions at small but finite  $\text{Re}$ , neglecting contributions of order  $\text{Re}^2$  and higher. The finite inertia of the fluid causes steady streaming flows (Figure 4a), which are

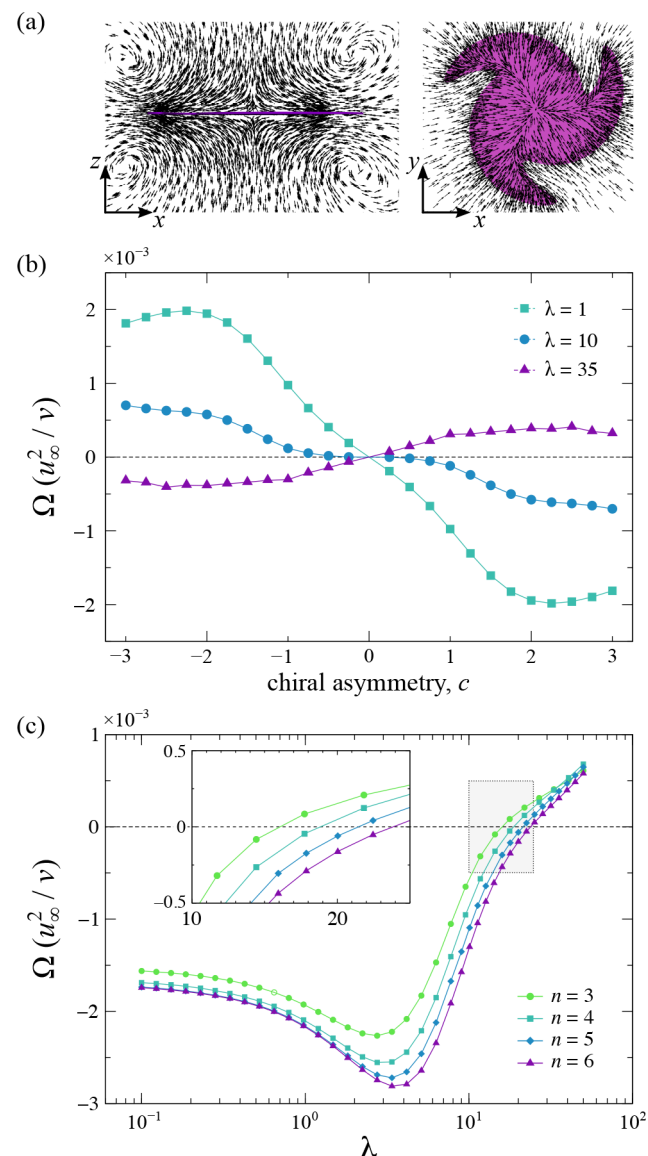


**Figure 4.** (a) Computed streaming flows around a 3-fin spinner as viewed from the side (left) or from the top (right). The chiral asymmetry parameter is  $c = 2$  ( $R$  spinner); the particle thickness is  $\delta = 0.02a$ ; the frequency parameter is  $\lambda = 5.1$ . (b) Computed angular velocity of the 3-fin spinner as a function of the chiral asymmetry for the different frequency parameters  $\lambda$ . (c) Computed angular velocity for  $R$  spinners ( $c = 2$ ) as a function of the frequency parameter  $\lambda$  for different numbers of fins  $n$ . The inset shows the crossover region where the rotation velocity changes sign.

superimposed on the leading order ( $\text{Re}^0$ ) oscillatory flows. These steady flows are accompanied by steady particle motions such that there is no net force or torque on the particle. The characteristics of the streaming flows and the associated particle motion depend strongly on the dimensionless frequency parameter  $\lambda = a(\omega/\nu)^{1/2}$ , which characterizes the ratio between the particle size  $a$  and the viscous boundary layer thickness  $(\nu/\omega)^{1/2}$ . In experiment, this parameter ranges from *ca.* 14 to 56 depending on the size of the particle.

Figure 4b shows the computed angular velocity  $\Omega$  (scaled by  $u_{\infty}^2/\nu$ ) for a 3-fin spinner of thickness  $\delta = 0.02a$  as a function of the chiral asymmetry  $c$ . For  $\lambda = 35$ , R spinners ( $c > 0$ ) rotate counterclockwise, and S spinners ( $c < 0$ ) rotate clockwise at speeds that increase with increasing asymmetry (cf. Figure 2b). The predicted rotation speed is comparable to that observed in experiment: for  $a = 5.8 \mu\text{m}$  (such that  $\lambda = 28$  and  $\text{Re} = 0.6$ ), the angular velocity is estimated to be  $\sim 4$  rad/s. We note that the predicted speeds are proportional to the square of the acoustic velocity (i.e.,  $\Omega \propto u_{\infty}^2$ ), which is known only to within an order of magnitude (see Methods). Given this uncertainty, we focus our attention on the qualitative features of the simulation results.

Figure 4c shows the computed angular velocity for R spinners ( $c = 2$ ) as a function of the frequency parameter  $\lambda$  for different numbers of fins  $n$ . The curves show similar qualitative behavior for all  $n$  considered. For small  $\lambda$  (i.e., at low frequencies or for small particles), spinners rotate in the CW direction with fins moving toward their convex side. The magnitude of the rotation velocity increases to a maximum at  $\lambda \approx 3$ . For higher  $\lambda$ , the rotation rate decreases monotonically and crosses zero at some value  $\lambda^* = \lambda^*(n)$  between ca. 14 and 24 for the model particles investigated here. The crossover point  $\lambda^*(n)$  is an increasing function of  $n$  in the studied range. Consequently, there exists some value  $\lambda_0$  such that  $\lambda^*(3) < \lambda_0 < \lambda^*(4)$ . At this value, a 3-fin R spinner is predicted to rotate in the CCW direction ( $\Omega > 0$ ) while spinners with more fins ( $n > 3$ ) rotate in the opposite direction ( $\Omega < 0$ ; Figure S1). This result is consistent with the velocity reversal observed experimentally for R spinners on increasing the number of fins from 3 to 4 (cf. Figure 3a).

The model does not, however, explain why the 6-fin spinner rotates again in the same direction as the 3-fin spinner (Figure 3a). One possible explanation for this discrepancy is that the crossover values  $\lambda^*$  depend sensitively on the particle geometry. Simulations of thinner ( $\delta = 0.02a$ ) and thicker ( $\delta = 0.1a$ ) spinners show significant differences in  $\Omega$  in the vicinity of the crossover region (cf. Figure 4 and Figure S2). Subtle differences between the model particles and those used in experiment may contribute to qualitative differences in particle dynamics in this parameter region (e.g., square vs rounded corners). Additionally, the model assumes small but finite Reynolds number and neglects contributions of  $O(\text{Re}^2)$  and higher. Higher-order inertial effects may be significant in experiments, for which the Reynolds number is of order unity. This fact could also explain why the model predictions disagree with the experimentally observed dependence of the rotation rate on particle size. In particular, experiment shows that the CCW rotation rate of 3-fin spinners decreases with the increasing  $\lambda$  (see Figure 3b where  $a \propto \lambda$ ), whereas the model predicts just the opposite trend (see Figure 4c, the region of largest  $\lambda$ ).

Physically, the rotation reversal predicted theoretically at  $\lambda \sim 10$  marks the transition between two qualitatively different frequency regimes. In the low-frequency regime ( $\lambda \ll 1$ ), inertial effects are significant only at large distances  $O(a\lambda^{-1})$  from the particle.<sup>39</sup> At high frequencies ( $\lambda \gg 1$ ), the flow around the particle is inviscid except for the thin boundary layer near the particle surface.<sup>39</sup> The transition from one regime to the other is accompanied by qualitative changes in the streaming flows, which follow more closely the contours of the particle as the frequency increases (Figure S3). Careful inspection of Figure 4c at the highest  $\lambda$  shows the crossing of  $\Omega(\lambda)$  curves for different  $n$ , highlighting the sensitive

dependence on particle shape in this regime (see also Figure S2).

**Translational Motions.** In the model, translational motion is prohibited due to the rotational symmetry of the particle and the uniformity of the acoustic field. In experiment, however, such motions were sometimes observed as illustrated in Figure 5a. In particular, we identified two types of translational motion

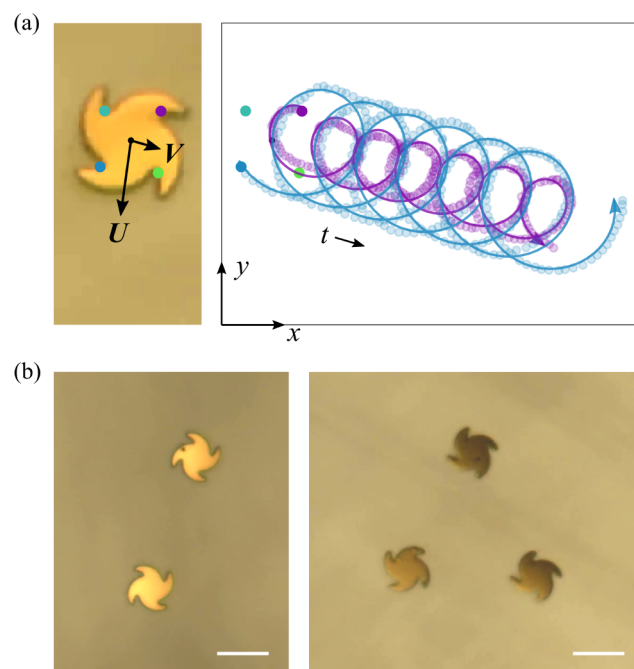


Figure 5. (a) Translational motions accompanying the rotation of a 4-armed spinner of radius  $a = 5.8 \mu\text{m}$  with chiral asymmetry  $c = -2$ . The image shows the position of the particle at time  $t = 0$ , with each corner identified by a colored marker. The plot shows reconstructed trajectories for two of the four corners (markers). The solid curves show the model trajectory with velocity  $U$  constant in the particle frame and velocity  $V$  constant in the particle frame; here,  $V = 1.6 \mu\text{m/s}$ ,  $U = 4.3 \mu\text{m/s}$ , and  $\Omega = 2.0$  rad/s (see Supporting Movie 4). (b) Particle interactions lead to a characteristic spacing of ca. three particle diameters between co-rotating spinners (see Supporting Movies 5–7); scale bars are  $15 \mu\text{m}$ .

in addition to the steady rotational motion detailed above. First, spinners moved with a velocity  $\mathbf{V}$  independent of their orientation as if acted upon by an external force. We attribute such motions to the spatial heterogeneity of the acoustic field, which leads to radiation forces directed parallel to the nodal plane.<sup>16,19</sup> Second, spinners moved with an additional velocity  $\mathbf{U}$ , which was constant in the particle frame of reference and changed direction as the particle rotated. Such motions are likely caused by defects in the particle that break its rotational symmetry and thereby enable self-propelled motions analogous to those of nanorods with  $C_{\infty v}$  symmetry.<sup>16,19</sup> Possible defects include warping of the thin spinners or the adsorption of an adventitious dust particle. Whatever the cause, these observations suggest that small defects in the particle shape can have a visible impact on its motion in the acoustic field.

## CONCLUSIONS

Controlling particle shape provides a versatile strategy for directing the motions of active particles powered by asymmetric acoustic streaming. While symmetry considerations alone can

identify possible particle motions, a detailed understanding of the propulsion mechanism and its dependence on particle shape is required to predict particle motions. The present experiments and simulations illustrate how particle motions can depend sensitively on particle shape under certain conditions. The ability to amplify subtle differences in particle shape (e.g., that of 3- and 4-armed spinners) into qualitative differences in particle motions is appealing for applications in separations and sensing. On the other hand, the simulations suggest other conditions, namely, smaller frequency parameters,  $\lambda < 10$ , for which particle motions are less sensitive to differences in particle shape (Figure 4).

Looking forward, there remain interesting questions as to how multiple spinners interact and organize to form dynamic assemblies. Figure 5b illustrates two primitive examples in which two and three co-rotating spinners form stationary assemblies characterized by an interparticle spacing of ca. 3 particle diameters (see Supporting Movies 5–7). This characteristic separation is hypothesized to originate through competition between hydrodynamic repulsion and acoustic confinement. The steady streaming flows surrounding each spinner are directed radially outward in the levitation plane causing particles to move away from one another; the acoustic radiation field creates confining potentials that act to push particles into localized nodal regions. In contrast to similar assemblies of rotating particles in 2D (e.g., those driven by magnetic fields<sup>40</sup>), the present assemblies do not rotate owing to the absence of external torques. Unfortunately, the observation of such assemblies was rare owing to the irreversible aggregation of spinners on contact with one another; further exploration of spinner assemblies will require additional strategies for mitigating particle aggregation. Mixtures of counter-rotating colloids are predicted to exhibit a variety of dynamic behaviors such as activity-induced phase separation<sup>30</sup> and the emergence of collective excitations such as vortex doublets.<sup>32</sup> Shape-directed particle motions powered by ultrasound should provide an attractive route to explore these and other interesting predictions of colloidal organization outside of equilibrium.

## METHODS

**Experimental. Fabrication of Spinners.** Gold spinners were fabricated by projection lithography using an I-line (365 nm light) GCA 8500 stepper. Prior to exposure, a sacrificial layer of silver (70 nm thickness) was deposited onto a 10 cm silicon wafer (single side polished, B-doped, 450  $\mu\text{m}$  thick, Virginia Semiconductor) by thermal evaporation. Successive layers of positive photoresist (ca. 1  $\mu\text{m}$  of LOR 5A and ca. 0.5  $\mu\text{m}$  of SPR 3012) were then deposited by spin-coating and soft baking at 180  $^{\circ}\text{C}$  for 2 min and at 95  $^{\circ}\text{C}$  for 1 min, respectively. Following UV exposure through the patterned mask, the photoresist was developed in MF CD-26 for 1 min, rinsed in deionized water, and dried in a nitrogen stream to create spinner-shaped wells. Approximately 150 nm of gold was then deposited onto the patterned wafer by thermal evaporation. The gold-covered photoresist was stripped using Remover PG to reveal the gold particles adhered to the silver layer. Finally, the wafer was soaked in 8 M nitric acid to dissolve the sacrificial layer and sonicated to release the spinners.

**Acoustic Chamber.** Experiments were conducted using the same acoustic chamber described in previous studies.<sup>16,19</sup> The chamber was constructed from a stainless steel plate (4.2 cm  $\times$  4.2 cm  $\times$  1 mm) covered on one side with several layers of Kapton tape. A circular hole was punched in the center of the tape to create a cylindrical chamber of height  $h = 180 \mu\text{m}$  and diameter  $D = 5 \text{ mm}$ . A piezoelectric transducer (1 mm thick, PZ26 Ferroperm, Kvistgard, Denmark) was attached on the opposite side of the steel plate using epoxy. Prior to

operation, the chamber was filled with a dispersion of spinners (ca. 30  $\mu\text{L}$ ) in water at room temperature and capped with a square glass coverslip. The resonant frequency of 3.77 MHz was determined empirically by tuning the signal frequency and observing the levitation and axial motion of nanorods at the center of the cell.<sup>16</sup> In all experiments, the magnitude of the harmonic signal input to the transducer was 10 V peak-to-peak. Particle dynamics were captured by a digital camera mounted to Olympus BX60 light microscope operating in reflected light mode.

**Acoustic Velocity.** The magnitude of the standing acoustic wave within the resonant chamber is difficult to measure directly. It is therefore common to infer the acoustic pressure and velocity from the radiation-induced motion of colloidal particles within the chamber. In this way, the primary radiation force on a gold nanorod (2  $\mu\text{m}$  long and 300 nm in diameter) was previously estimated to be  $F_{\text{rad}} = 0.7 \text{ pN}$ .<sup>16</sup> Approximating the nanorod as a dense, incompressible sphere of radius  $a = 1 \mu\text{m}$  in a one-dimensional standing wave, the radiation force can be related to the acoustic pressure  $p_a$  as  $F_{\text{rad}} = \frac{5}{6}\pi(ka^3p_a^2/\rho c^2)$ , where  $k$  is the wavenumber,  $\rho$  is the fluid density, and  $c$  is the speed of sound.<sup>41</sup> Using this expression, the acoustic pressure is estimated to be  $p_a \sim 200 \text{ kPa}$ , and the acoustic velocity  $u^\infty = p_a/\rho c \sim 0.1 \text{ m/s}$ . At the driving frequency of 3.77 MHz, such velocities correspond to an amplitude of  $u^\infty/\omega \sim 5 \text{ nm}$ , much smaller than the particle. These order of magnitude estimates are useful in comparing the quantitative predictions of the theoretical model with the experimental observations.

**Measurement of Particle Velocity.** Particle tracking was performed manually using Fiji<sup>42</sup> to identify the positions of the  $n$  fin tips at successive frames for at least two particle revolutions. From these data, we computed the position  $(x, y)$  and orientation  $\theta$  of the particle as a function of time. As shown in Figure 2a, the average angular velocity  $\Omega$  was determined by linear regression of the  $\theta$  vs  $t$  data. In Figures 2b and 3, the average angular velocity was instead computed as  $\Omega = 2\pi N/T$ , where  $N \geq 2$  is the number of revolutions within a given period  $T$ . In Figure 5a, the trajectories of the particle corners were reconstructed automatically using TrackPy; the quoted velocities were obtained by fitting the observed trajectories to the kinematic model using least-squares regression.

**Hydrodynamic Model.** Following Nadal and Lauga,<sup>26</sup> we consider the motion of a solid particle in a fluid subject to an oscillating velocity field. Owing to the difference in density between the particle and the fluid, the particle will move relative to the fluid, inducing transient flows governed by the Navier–Stokes equations

$$\rho \left( \frac{\partial \mathbf{u}}{\partial t} + \mathbf{u} \cdot \nabla \mathbf{u} \right) = -\nabla p + \eta \nabla^2 \mathbf{u} \text{ and } \nabla \cdot \mathbf{u} = 0 \quad (2)$$

At the surface of the particle  $\mathcal{S}$ , the no-slip condition implies that the fluid moves with the velocity of the particle

$$\mathbf{u}(\mathbf{x}, t) = \mathbf{U}(t) + \boldsymbol{\Omega}(t) \times (\mathbf{x} - \mathbf{x}_p(t)) \text{ for } \mathbf{x} \in \mathcal{S} \quad (3)$$

where  $\mathbf{U}$  and  $\boldsymbol{\Omega}$  are the linear and angular velocity of the particle and  $\mathbf{x}_p$  is its center of mass. Far from the particle, the velocity oscillates with frequency  $\omega$  and magnitude  $\hat{u}^\infty$

$$\mathbf{u}(\mathbf{x}, t) = \mathcal{R}(\hat{\mathbf{u}}^\infty e^{-i\omega t}) \text{ for } |\mathbf{x} - \mathbf{x}_p| \rightarrow \infty \quad (4)$$

This oscillating flow in the far-field describes the effects of the acoustic field for particles moving at the nodal plane.<sup>26</sup> We assume the fluid oscillates in the  $z$ -direction of the laboratory frame,  $\hat{\mathbf{u}}^\infty = \hat{u}^\infty \mathbf{e}_z$ . Together, eqs 2–4 specify the motion of the fluid around the particle.

Additionally, the rigid body motion of the particle is governed by

$$m \frac{d\mathbf{U}}{dt} = \mathbf{F}_H \text{ and } \frac{d}{dt}(\mathbf{I} \cdot \boldsymbol{\Omega}) = \mathbf{L}_H \quad (5)$$

where  $m$  is the mass of the particle and  $\mathbf{I}$  is its inertia tensor.<sup>43</sup> The hydrodynamic force and torque on the particle are obtained by integrating the hydrodynamic stresses over the particle surface

$$\mathbf{F}_H(t) = \int_S (\boldsymbol{\sigma} \cdot \mathbf{n}) dS \quad (6)$$

$$\mathbf{L}_H(t) = \int_S (\mathbf{x} - \mathbf{x}_p) \times (\boldsymbol{\sigma} \cdot \mathbf{n}) dS \quad (7)$$

where  $\boldsymbol{\sigma} = -p\boldsymbol{\delta} + \eta(\nabla\mathbf{u} + \nabla\mathbf{u}^T)$  is the stress tensor and  $\mathbf{n}$  is the unit normal vector directed out from the particle surface. Together with the kinematics of rigid body motion, the above equations fully specify the translational and rotational motion of the particle.

It is convenient to nondimensionalize the above problem by scaling time by  $\omega^{-1}$ , length by  $a$ , velocity by  $u^\infty$ , pressure by  $\eta u^\infty/a$ , force by  $6\pi\eta a u^\infty$ , and torque by  $6\pi\eta a^2 u^\infty$ . The dimensionless equations are then characterized by three dimensionless parameters: the Reynolds number,  $\text{Re} = \rho a u^\infty/\eta$ ; the frequency parameter,  $\lambda^2 = a^2 \omega \rho/\eta$ ; and the Stokes number  $\text{St} = m\omega/6\pi\eta a$ . In experiment, the far-field velocity is estimated to be  $u^\infty = 0.1$  m/s (see above). This estimate corresponds to a Reynolds number of  $\text{Re} = 0.6$  (for  $a = 5.8$   $\mu\text{m}$ ), which is not much smaller than unity. Nevertheless, we expand our solutions for the (dimensionless) fluid velocity and pressure in a Taylor series with the Reynolds number as the small parameter

$$\mathbf{u}(\mathbf{x}, t) = \mathbf{u}^{(0)}(\mathbf{x}, t) + \text{Re} \mathbf{u}^{(1)}(\mathbf{x}, t) + \dots \quad (8)$$

$$p(\mathbf{x}, t) = p^{(0)}(\mathbf{x}, t) + \text{Re} p^{(1)}(\mathbf{x}, t) + \dots \quad (9)$$

For simplicity, we use the same notations for both the dimensional and the dimensionless quantities. Additionally, we assume the simplest particle kinematics permitted by the symmetry of the particle and the external velocity field. In particular, we consider only those motions in which the particle axis is exactly perpendicular to the nodal plane and parallel to the oscillating flow such that  $\mathbf{U}(t) = U(t)\mathbf{e}_z$  and  $\boldsymbol{\Omega}(t) = \Omega(t)\mathbf{e}_z$ .

At zeroth order in the Reynolds number, the flow is purely oscillatory  $\mathbf{u}^{(0)} = \mathcal{R}(\hat{\mathbf{u}}^{(0)} e^{-it})$  and  $p^{(0)} = \mathcal{R}(\hat{p}^{(0)} e^{-it})$  with Fourier components  $\hat{\mathbf{u}}^{(0)}$  and  $\hat{p}^{(0)}$  governed by

$$-i\lambda^2 \hat{\mathbf{u}}^{(0)} = -\nabla \hat{p}^{(0)} + \nabla^2 \hat{\mathbf{u}}^{(0)} \text{ and } \nabla \cdot \hat{\mathbf{u}}^{(0)} = 0 \quad (10)$$

The frequency parameter is estimated to be  $\lambda^2 = O(10^3) \gg 1$ , which implies that the viscous boundary layer is much thinner than the particle radius. We note that this regime is the opposite of that considered previously by Nadal and Lauga.<sup>26</sup> At this order, the boundary conditions become

$$\hat{\mathbf{u}}^{(0)}(\mathbf{x}) = \mathbf{e}_z \text{ for } |\mathbf{x} - \mathbf{x}_p| \rightarrow \infty \quad (11)$$

$$\hat{\mathbf{u}}^{(0)}(\mathbf{x}) = \hat{U}^{(0)} \mathbf{e}_z \text{ for } \mathbf{x} \in S \quad (12)$$

where  $\hat{U}^{(0)}$  is related to  $U^{(0)}(t)$  through  $U^{(0)}(t) = \mathcal{R}(\hat{U}^{(0)} e^{-it})$ . The particle velocity in the  $z$ -direction is coupled to the fluid motion as

$$-i\text{St} \hat{U}^{(0)} = \hat{F}_H^{(0)} \quad (13)$$

In experiment, the Stokes number is estimated to be  $\text{St} = 70 \gg 1$ , which suggests that the velocity of the particle is small relative to that of the fluid. To simplify our analysis, we neglect the small oscillatory motions of the particle and set  $\hat{U}^{(0)} = 0$  (as well as  $\hat{U}^{(1)} = 0$ ). The zeroth-order flow field is solved numerically using the boundary element method (see below).

At first order in the Reynolds number, the zeroth order oscillatory flow induces a steady streaming flow  $\mathbf{u}^{(1)}$  governed by

$$-\nabla p^{(1)} + \nabla^2 \mathbf{u}^{(1)} = \frac{1}{4} [(\hat{\mathbf{u}}^{(0)} \cdot \nabla) \hat{\mathbf{u}}^{(0)} + (\hat{\mathbf{u}}^{(0)} \cdot \nabla) \hat{\mathbf{u}}^{(0)}] \text{ and } \nabla \cdot \mathbf{u}^{(1)} = 0 \quad (14)$$

where complex conjugate quantities are underlined;<sup>26</sup> note that  $\mathbf{u}^{(1)}$  denotes only the steady component of the first-order flow field. At this order, there is no net force or torque on the particle; however, the particle is expected to rotate about its axis at a constant rate. The fluid boundary conditions are therefore

$$\mathbf{u}^{(1)}(\mathbf{x}) = 0 \text{ for } |\mathbf{x} - \mathbf{x}_p| \rightarrow \infty \quad (15)$$

$$\mathbf{u}^{(1)}(\mathbf{x}) = \Omega^{(1)} \mathbf{e}_z \times (\mathbf{x} - \mathbf{x}_p) \text{ for } \mathbf{x} \in S \quad (16)$$

Here, the unknown angular velocity  $\Omega^{(1)}$  is determined by the zero torque condition

$$\mathbf{L}_H^{(1)} = 0 = \int_S (\mathbf{x} - \mathbf{x}_p) \times (\boldsymbol{\sigma}^{(1)} \cdot \mathbf{n}) dS \quad (17)$$

Rather than solve for the flow field directly, we make use of a suitable version of the Lorentz reciprocal theorem suggested by Nadal and Lauga.<sup>26</sup>

$$\Omega^{(1)} \bar{\mathbf{L}} = \frac{1}{4} \int_V \bar{\mathbf{u}} \cdot [(\hat{\mathbf{u}}^{(0)} \cdot \nabla) \hat{\mathbf{u}}^{(0)} + (\hat{\mathbf{u}}^{(0)} \cdot \nabla) \hat{\mathbf{u}}^{(0)}] dV \quad (18)$$

Here,  $\bar{\mathbf{u}}$  is an auxiliary velocity field associated with the steady rotation of the particle in a quiescent fluid subject to a torque,  $\bar{\mathbf{L}} = \bar{\mathbf{L}} \mathbf{e}_z$ . In dimensional units, the desired angular velocity is then given by  $(u^\infty/a) \text{Re} \Omega^{(1)}$ .

**Numerical Simulations.** Using the above model, the angular velocity of the particle and the accompanying fluid flow are computed numerically using the boundary element method (BEM).<sup>44</sup> The computation is divided into two steps: first we solve eqs 10–12 for the oscillatory Stokes flow  $\hat{\mathbf{u}}^{(0)}$ ; we then compute the auxiliary Stokes flow and the angular velocity  $\Omega^{(1)}$  using eq 18. As detailed below, the first step relies on a boundary integral formulation for oscillatory Stokes flows.<sup>45</sup> The second step makes use of the standard BEM for steady Stokes flows.<sup>44</sup>

The zeroth-order flow field  $\hat{\mathbf{u}}^{(0)}$  can be expressed as the external flow due to the acoustic field less some disturbance field due to the particle

$$\hat{\mathbf{u}}^{(0)} = \mathbf{e}_z - \hat{\mathbf{u}}^T \quad (19)$$

The disturbance velocity  $\hat{\mathbf{u}}^T$  represents the flow due to an oscillating particle in an unbounded quiescent fluid. To calculate the disturbance field, we employ an integral representation for the unsteady Stokes problem in terms of the “single-layer” distribution<sup>45</sup>

$$\hat{\mathbf{u}}_k^T(\mathbf{x}) = -\frac{1}{8\pi} \int_S \hat{q}_j(\mathbf{x}') \hat{G}_{jk}(\mathbf{x} - \mathbf{x}') dS(\mathbf{x}') \quad (20)$$

This representation is valid for points  $\mathbf{x}$  in the fluid and at the particle surface. In eq 20,  $\hat{q} \equiv \hat{\boldsymbol{\sigma}}^{(0)} \cdot \mathbf{n} + i\lambda^2 z \mathbf{n}$  is the unknown distribution on the particle surface, and  $\hat{G}_{jk}(\mathbf{x} - \mathbf{x}')$  is the Green's function for the unsteady Stokes eq 10. This function represents the fluid velocity at  $\mathbf{x}$  due to an oscillating Stokeslet at  $\mathbf{x}'$ <sup>45</sup>

$$\hat{G}_{jk}(\mathbf{x}) = \frac{\delta_{jk}}{|\mathbf{x}|} A(\sqrt{-i}\lambda|\mathbf{x}|) + \frac{x_j x_k}{|\mathbf{x}|^3} B(\sqrt{-i}\lambda|\mathbf{x}|) \quad (21)$$

where  $\delta_{jk}$  is the Kronecker delta, and the functions  $A$  and  $B$  are defined as

$$A(z) = 2e^{-z} \left( 1 + \frac{1}{z} + \frac{2}{z^2} \right) - \frac{2}{z^2} \quad (22)$$

$$B(z) = -2e^{-z} \left( 1 + \frac{3}{z} + \frac{3}{z^2} \right) + \frac{6}{z^2} \quad (23)$$

Given the fluid velocity at the particle surface (i.e.,  $\hat{\mathbf{u}}^T(\mathbf{x}) = \mathbf{e}_z$  for  $\mathbf{x} \in S$ ), the integral eq 20 for the unknown distribution  $\hat{q}$  is solved numerically using the BEM.<sup>44</sup>

The surfaces of the spinners as well as the volume  $\mathcal{V}$  in eq 18 are discretized using the open source Quality Tetrahedral Mesh Generator (TetGen) library.<sup>46</sup> TetGen generates boundary conforming Delaunay meshes of three-dimensional domains delimited by piecewise linear boundaries. Adaptive mesh refinement with isotropic size conforming triangulation is used to create nonuniform meshes, which have progressively smaller elements close to the particle surface. The surface meshes used in this work have ca.  $2 \times 10^4$  triangles (Figure S4); meshes over the large (but finite) volume  $\mathcal{V} = (400a)^3$  have ca.  $5 \times$

$10^5$  elements. The volume integral in eq 18 is carried out using a finite element approach with linear tetrahedral elements; integration over the elements is performed numerically using fully symmetric Gaussian quadrature rules.<sup>47</sup>

## ASSOCIATED CONTENT

### Supporting Information

The Supporting Information is available free of charge on the ACS Publications website at DOI: 10.1021/acsnano.8b00525.

Description of supplemental movies; computed angular velocity showing rotation reversal with increasing number of fins  $n$ ; computed angular velocity for thicker spinners ( $\delta = 0.1a$ ); computed streaming flows for a 3-armed spinner; sample surface mesh for a 3-armed spinner (PDF)

Movie 1 (MP4)

Movie 2 (MP4)

Movie 3 (MP4)

Movie 4 (MP4)

Movie 5 (MP4)

Movie 6 (MP4)

Movie 7 (MP4)

## AUTHOR INFORMATION

### Corresponding Author

\*E-mail: kyle.bishop@columbia.edu.

### ORCID

Kyle J. M. Bishop: 0000-0002-7467-3668

### Notes

The authors declare no competing financial interest.

## ACKNOWLEDGMENTS

This work was supported as part of the Center for Bio-Inspired Energy Science, an Energy Frontier Research Center funded by the U.S. Department of Energy, Office of Science, Basic Energy Sciences under Award DE-SC0000989. M.T. acknowledges financial support from the Portuguese Foundation for Science and Technology (FCT) under Contract No. IF/00322/2015. A.M.B. was supported in part by the National Science Foundation Graduate Research Fellowship Program under Grant DGE1255832. S.A. was supported by the NSF-MRSEC Program under grant DMR-1420620.

## REFERENCES

- (1) Ebbens, S. J. Active colloids: Progress and Challenges Towards Realising Autonomous Applications. *Curr. Opin. Colloid Interface Sci.* **2016**, *21*, 14–23.
- (2) Li, J.; Rozen, I.; Wang, J. Rocket Science at the Nanoscale. *ACS Nano* **2016**, *10*, 5619–5634.
- (3) Dey, K. K.; Wong, F.; Altemose, A.; Sen, A. Catalytic Motors - *Quo Vadimus?* *Curr. Opin. Colloid Interface Sci.* **2016**, *21*, 4–13.
- (4) Paxton, W. F.; Kistler, K. C.; Olmeda, C. C.; Sen, A.; St. Angelo, S. K.; Cao, Y.; Mallouk, T. E.; Lammert, P. E.; Crespi, V. H. Catalytic Nanomotors: Autonomous Movement of Striped Nanorods. *J. Am. Chem. Soc.* **2004**, *126*, 13424–13431.
- (5) Fournier-Bidoz, S.; Arsenault, A. C.; Manners, I.; Ozin, G. A. Synthetic Self-Propelled Nanorotors. *Chem. Commun.* **2005**, 441–443.
- (6) Wang, Y.; Hernandez, R. M.; Bartlett, D. J.; Bingham, J. M.; Kline, T. R.; Sen, A.; Mallouk, T. E. Bipolar Electrochemical Mechanism for the Propulsion of Catalytic Nanomotors in Hydrogen Peroxide Solutions. *Langmuir* **2006**, *22*, 10451–10456.
- (7) Moran, J. L.; Wheat, P. M.; Posner, J. D. Locomotion of Electrocatalytic Nanomotors due to Reaction Induced Charge Autoelectrophoresis. *Phys. Rev. E* **2010**, *81*, 065302.

(8) Golestanian, R.; Liverpool, T. B.; Ajdari, A. Designing Phoretic Micro- and Nano-Swimmers. *New J. Phys.* **2007**, *9*, 126.

(9) Qin, L.; Banholzer, M. J.; Xu, X.; Huang, L.; Mirkin, C. A. Rational Design and Synthesis of Catalytically Driven Nanorotors. *J. Am. Chem. Soc.* **2007**, *129*, 14870–14871.

(10) Wang, Y.; Fei, S. T.; Byun, Y. M.; Lammert, P. E.; Crespi, V. H.; Sen, A.; Mallouk, T. E. Dynamic Interactions Between Fast Microscale Rotors. *J. Am. Chem. Soc.* **2009**, *131*, 9926–9927.

(11) Howse, J. R.; Jones, R. A. L.; Ryan, A. J.; Gough, T.; Vafabakhsh, R.; Golestanian, R. Self-Motile Colloidal Particles: From Directed Propulsion to Random Walk. *Phys. Rev. Lett.* **2007**, *99*, 048102.

(12) Michelin, S.; Lauga, E. Autophoretic Locomotion from Geometric Asymmetry. *Eur. Phys. J. E* **2015**, *38*, 91.

(13) Ma, F.; Wang, S.; Wu, D. T.; Wu, N. Electric Field-Induced Assembly and Propulsion of Chiral Colloidal Clusters. *Proc. Natl. Acad. Sci. U. S. A.* **2015**, *112*, 6307–6312.

(14) Maggi, C.; Saglimbeni, F.; Dipalo, M.; De Angelis, F.; Di Leonardo, R. Micromotors with Asymmetric Shape that Efficiently Convert Light into Work by Thermocapillary Effects. *Nat. Commun.* **2015**, *6*, 7855.

(15) Klotsa, D.; Baldwin, K. A.; Hill, R. J. A.; Bowley, R. M.; Swift, M. R. Propulsion of a Two-Sphere Swimmer. *Phys. Rev. Lett.* **2015**, *115*, 248102.

(16) Wang, W.; Castro, L. A.; Hoyos, M.; Mallouk, T. E. Autonomous Motion of Metallic Microrods Propelled by Ultrasound. *ACS Nano* **2012**, *6*, 6122–6132.

(17) Ahmed, S.; Wang, W.; Mair, L. O.; Fraleigh, R. D.; Li, S.; Castro, L. A.; Hoyos, M.; Huang, T. J.; Mallouk, T. E. Steering Acoustically Propelled Nanowire Motors Toward Cells in a Biologically Compatible Environment Using Magnetic Fields. *Langmuir* **2013**, *29*, 16113–16118.

(18) Ahmed, S.; Gentekos, D. T.; Fink, C. A.; Mallouk, T. E. Self-Assembly of Nanorod Motors into Geometrically Regular Multimers and Their Propulsion by Ultrasound. *ACS Nano* **2014**, *8*, 11053–11060.

(19) Ahmed, S.; Wang, W.; Bai, L.; Gentekos, D. T.; Hoyos, M.; Mallouk, T. E. Density and Shape Effects in the Acoustic Propulsion of Bimetallic Nanorod Motors. *ACS Nano* **2016**, *10*, 4763–4769.

(20) Garcia-Gradilla, V.; Orozco, J.; Sattayasamitsathit, S.; Soto, F.; Kuralay, F.; Pourazary, A.; Katzenberg, A.; Gao, W.; Shen, Y.; Wang, J. Functionalized Ultrasound-Propelled Magnetically Guided Nanomotors: Toward Practical Biomedical Applications. *ACS Nano* **2013**, *7*, 9232–9240.

(21) Wang, W.; Li, S.; Mair, L.; Ahmed, S.; Huang, T. J.; Mallouk, T. E. Acoustic Propulsion of Nanorod Motors Inside Living Cells. *Angew. Chem.* **2014**, *126*, 3265–3268.

(22) Xu, T.; Soto, F.; Gao, W.; Dong, R.; Garcia-Gradilla, V.; Magana, E.; Zhang, X.; Wang, J. Reversible Swarming and Separation of Self-propelled Chemically-Powered Nanomotors under Acoustic Fields. *J. Am. Chem. Soc.* **2015**, *137*, 2163–2166.

(23) Rao, K. J.; Li, F.; Meng, L.; Zheng, H.; Cai, F.; Wang, W. A Force to Be Reckoned With: A Review of Synthetic Microswimmers Powered by Ultrasound. *Small* **2015**, *11*, 2836–2846.

(24) Balk, A. L.; Mair, L. O.; Mathai, P. P.; Patrone, P. N.; Wang, W.; Ahmed, S.; Mallouk, T. E.; Liddle, J. A.; Stavis, S. M. Kilohertz Rotation of Nanorods Propelled by Ultrasound, Traced by Microvortex Advection of Nanoparticles. *ACS Nano* **2014**, *8*, 8300–8309.

(25) Wang, W.; Duan, W.; Zhang, Z.; Sun, M.; Sen, A.; Mallouk, T. E. A Tale of Two Forces: Simultaneous Chemical and Acoustic Propulsion of Bimetallic Micromotors. *Chem. Commun.* **2015**, *51*, 1020–1023.

(26) Nadal, F.; Lauga, E. Asymmetric Steady Streaming as a Mechanism for Acoustic Propulsion of Rigid Bodies. *Phys. Fluids* **2014**, *26*, 082001.

(27) Bricard, A.; Caussin, J.-B.; Das, D.; Savoie, C.; Chikkadi, V.; Shitara, K.; Chepizhko, O.; Peruani, F.; Saintillan, D.; Bartolo, D. Emergent Vortices in Populations of Colloidal Rollers. *Nat. Commun.* **2015**, *6*, 7470.

- (28) Snezhko, A. Complex Collective Dynamics of Active Torque-Driven Colloids at Interfaces. *Curr. Opin. Colloid Interface Sci.* **2016**, *21*, 65–75.
- (29) Kaiser, A.; Snezhko, A.; Aranson, I. S. Flocking Ferromagnetic Colloids. *Sci. Adv.* **2017**, *3*, e1601469.
- (30) Nguyen, N. H. P.; Klotsa, D.; Engel, M.; Glotzer, S. C. Emergent Collective Phenomena in a Mixture of Hard Shapes through Active Rotation. *Phys. Rev. Lett.* **2014**, *112*, 75701.
- (31) Spellings, M.; Engel, M.; Klotsa, D.; Sabrina, S.; Drews, A. M.; Nguyen, N. H. P.; Bishop, K. J. M.; Glotzer, S. C. Shape Control and Compartmentalization in Active Colloidal Cells. *Proc. Natl. Acad. Sci. U. S. A.* **2015**, *112*, E4642–E4650.
- (32) Sabrina, S.; Spellings, M.; Glotzer, S. C.; Bishop, K. J. M. Coarsening Dynamics of Binary Liquids with Active Rotation. *Soft Matter* **2015**, *11*, 8409–8416.
- (33) Yeo, K.; Lushi, E.; Vlahovska, P. M. Collective Dynamics in a Binary Mixture of Hydrodynamically Coupled Microrotors. *Phys. Rev. Lett.* **2015**, *114*, 188301.
- (34) Yeo, K.; Lushi, E.; Vlahovska, P. M. Dynamics of Inert Spheres in Active Suspensions of Micro-Rotors. *Soft Matter* **2016**, *12*, 5645–5652.
- (35) Snezhko, A.; Aranson, I. S. Magnetic Manipulation of Self-Assembled Colloidal Asters. *Nat. Mater.* **2011**, *10*, 698–703.
- (36) Martinez-Pedrero, F.; Tierno, P. Magnetic Propulsion of Self-Assembled Colloidal Carpets: Efficient Cargo Transport via a Conveyor-Belt Effect. *Phys. Rev. Appl.* **2015**, *3*, 051003.
- (37) Brooks, A. M.; Sabrina, S.; Bishop, K. Shaped-Directed Dynamics of Active Colloids Powered by Induced-Charge Electrophoresis. *Proc. Natl. Acad. Sci. U. S. A.* **2018**, *115*, E1090–E1099.
- (38) Han, K.; Shields, C. W.; Velez, O. D. Engineering of Self-Propelling Microbots and Microdevices Powered by Magnetic and Electric Fields. *Adv. Funct. Mater.* **2017**, 1705953.
- (39) Zhang, W.; Stone, H. Oscillatory Motions of Circular Disks and Nearly Spherical Particles in Viscous Flows. *J. Fluid Mech.* **1998**, *367*, 329–358.
- (40) Grzybowski, B. A.; Stone, H. A.; Whitesides, G. M. Dynamic Self-Assembly of Magnetized, Millimetre-Sized Objects Rotating at a Liquid-Air Interface. *Nature* **2000**, *405*, 1033–1036.
- (41) Bruus, H. Acoustofluidics 7: The Acoustic Radiation Force on Small Particles. *Lab Chip* **2012**, *12*, 1014–21.
- (42) Schindelin, J.; Arganda-Carreras, I.; Frise, E.; Kaynig, V.; Longair, M.; Pietzsch, T.; Preibisch, S.; Rueden, C.; Saalfeld, S.; Schmid, B.; Tinevez, J.-Y.; White, D. J.; Hartenstein, V.; Eliceiri, K.; Tomancak, P.; Cardona, A. Fiji: An Open-Source Platform for Biological Image Analysis. *Nat. Methods* **2012**, *9*, 676–682.
- (43) Landau, L. D.; Lifshitz, E. M. *Mechanics*; Butterworth-Heinemann: New York, 1976.
- (44) Pozrikidis, C. *A Practical Guide to Boundary Element Methods with the Software Library BEMLIB*; CRC Press: Boca Raton, FL, 2002.
- (45) Pozrikidis, C. A study of Linearized Oscillatory Flow Past Particles by the Boundary-Integral Method. *J. Fluid Mech.* **1989**, *202*, 17–41.
- (46) Si, H. TetGen: A Delaunay-Based Quality Tetrahedral Mesh Generator. *ACM Trans. on Mathematical Software* **2015**, *41*, 1.
- (47) Cools, R. An Encyclopaedia of Cubature Formulas. *J. Complexity* **2003**, *19*, 445–453.